Appendices

Appendix A.

Remote Sensing Field Methods

1 Photogrammetry

Digital photogrammetry applies the principles of stereoscopy to create 3-D models from overlapping 2-D photographs taken from offset camera stations (Figure 3 - 1).

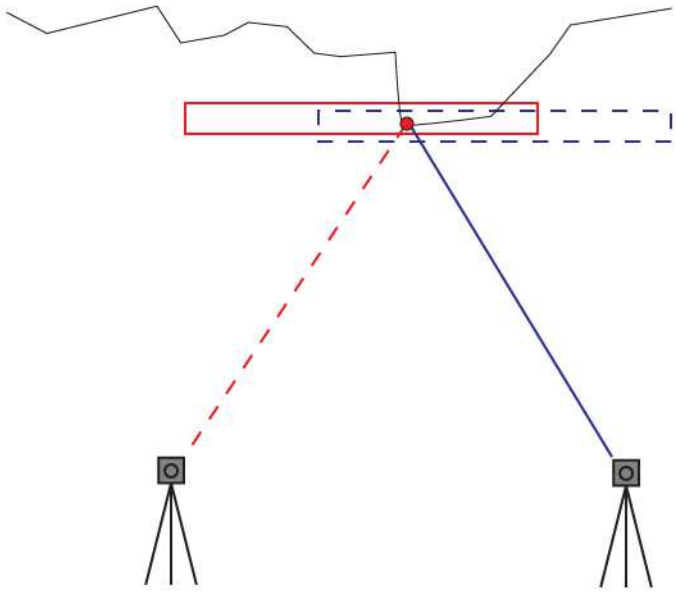

Figure 3 - 1: Point-matching on corresponding photographs from offset camera stations allows the 3-D location of points to be computed.

Photogrammetry software provides an automated workflow that includes two main mathematical processes in order to construct 3-D terrain models from 2-D images. Birch (2006) summarises the processes:

(1) **Image matching** is first done automatically by the software, which scans through a set of overlapping images in order to identify the relative locations of corresponding points in images from offset camera stations (Figure 3 - 1)

(2) **Exterior orientation** can then be automatically computed, describing the separation between perspective centres of offset camera stations, and the rotation of the camera at each station

a) *Absolute orientation* can be achieved when images are registered with respect to a real-world coordinate system, usually by manual identification of surveyed control points on corresponding images

b) *Relative orientation* can be used if no control points are available; in this case the 3-D model is registered in an arbitrary coordinate system; the terrain model may still be scaled by providing known separation distance between camera stations, or by identifying a known scale bar in the image set.

Once the 3-D location of each pixel is computed, the software can construct a point cloud relating to the location of each pixel, or a 3-D meshed surface called a digital terrain model (DTM), with photograph overlays to display surface colour.

For this study, long-range surveys (i.e. photographed from distances exceeding approximately 500 m) were undertaken using a high focal length telephoto lens (f = 100 mm to f = 400 mm), configured in an image fan layout (Figure 3 - 2), as proposed for use in surveying open pit mines and natural rock slopes by Sturzenegger and Stead (2012, 2009b), Sturzenegger (2010), and Lee (2011). Close-range surveys (i.e. photographed from distances less than approximately 50 m) for use in 2-D digital trace mapping were taken using an f = 20 mm fixed focal length (prime) lens.

Registration of the 3-D terrain models in local mine coordinates was achieved by identifying geodetic prisms with known coordinates. All three mines have pre-existing arrays of geodetic prisms installed at bench crest locations, used for slope movement monitoring by robotic total station. By manually identifying sets of 6 or more prisms on successive 2-D images (Birch, 2006), the photogrammetry software can automatically produce an alignment matrix, which applies rotation and translation of the full DTM to local mine coordinates.

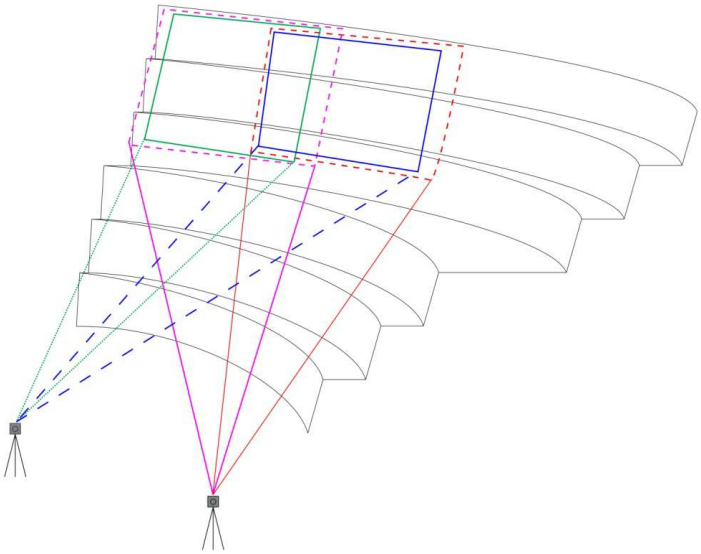

Figure 3 - 2: Example of image fan layout for long-range open pit slope photogrammetry, with bench heights of 30 m and an overall slope height of 180 m.

This thesis focuses on observations from photogrammetry at 2 mines and an outcrop near Squamish, BC. Photographs were taken using a Canon EOS 5D Mark II digital SLR camera, with an adjustable Canon EF *f* = 100 - 400 mm telephoto lens (Figure 3 - 3).

Figure 3 - 3: Canon EOS 5D Mark II camera body, and EL 100 mm – 400 mm telephoto lens.

The ground pixel size of a photogrammetry survey is a function of the focal length of the camera lens, the shooting distance to the rock face, and the dimensions of the camera's image sensor (Figure 3 - 4):

$$\boldsymbol{Ground\ Point\ Resolution} = Pixel\ size\ on\ face = \frac{d}{f} \times (pixel\ size\ on\ image\ sensor)$$

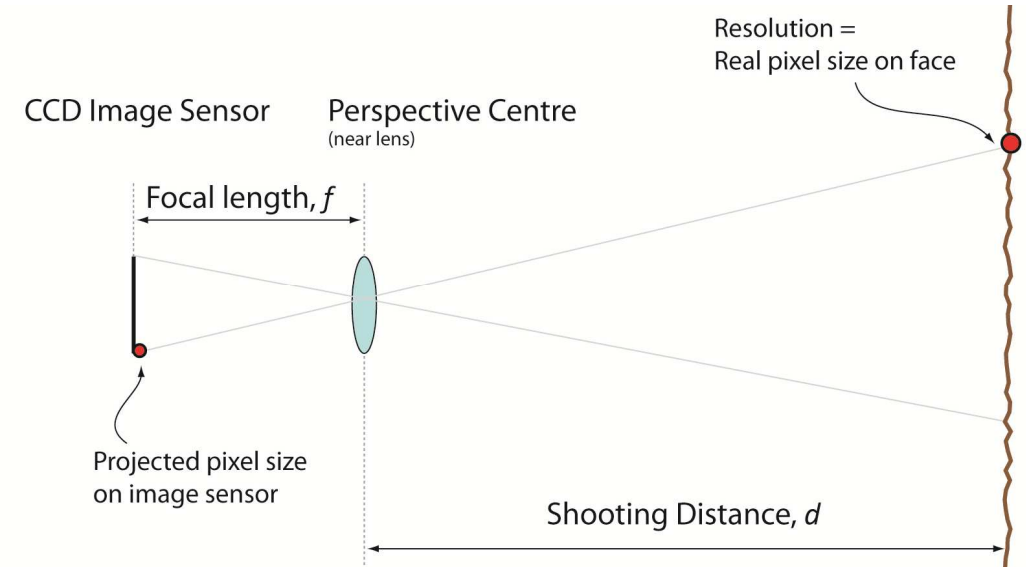

Figure 3 - 4: Schematic illustration of factors influencing photogrammetry survey resolution (Modified and reproduced after Birch, 2006)

Whereas resolution quantifies the precision of a photogrammetry survey, accuracy quantifies the potential error in projected location of a point on the DTM, relative to its true location in real-world space (Birch, 2006; Sturzenegger, 2010).

- **Planimetric accuracy** describes the potential in-plane error, parallel to the camera image sensor, and is dependent on ground pixel size and an image accuracy factor $\boldsymbol{\delta_{pixel}}$ which is automatically calculated by the photogrammetry software.
    - Image accuracy $\boldsymbol{\delta_{pixel}}$ in turn depends on the quality of the successive images being stereo-matched, and the calibration of distortion corrections for a specific camera-lens combination.
- **Depth accuracy** is a function of planimetric accuracy, and separation distance between camera stations:

$$\delta_{depth} = \frac{shooting\ distance}{camera\ station\ separation}\delta_{plan}$$

ADAM Technology (2010) recommends shooting distance/camera station separation ratios ranging from about 2/1 to 6/1, and cautions that ratios outside 1/1 to 10/1 cause problems for the image-matching function.

In photogrammetry models, calibration was undertaken for each camera/lens combination, with focal length fixed at infinity. The result is a set of calibration parameters including: radial lens distortion factors (termed K1, K2, K3, K4); offset of the image censor centre, in X and Y directions (termed Xp, Yp); decentring distortion (termed P1, P2); and scaling factor distortion (B1, B2). The resultant calibration can be visualized with an interference pattern (Figure 3 - 5) that illustrates the increasing distortion with radial distance away from the centre of the image (Adam Technology, 2010).

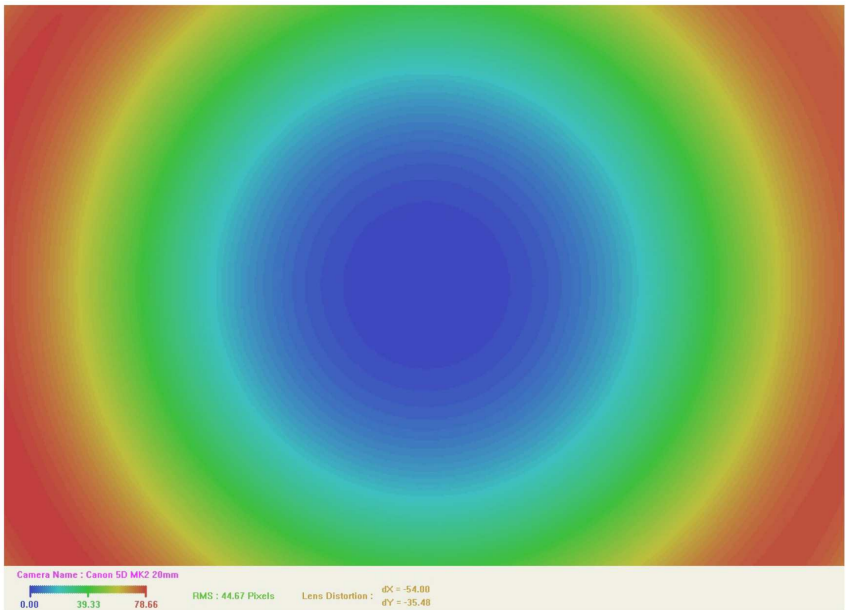

Figure 3 - 5: Interference pattern for Canon 5D Mark II with *f* = 20 mm prime lens.

2 LiDAR

LiDAR (LIght Detection And Ranging) survey measures reflected laser beams to generate a 3-D point cloud of a target. Most LiDAR scanners use either of two methods for range calculation:

- **Phase method** scanners emit a continuous laser beam comprised of two or more superimposed signals: a carrier signal and one or more modulation signals. As the reflected beam returns to the scanner, the phase-shift (expressed as a distance or partial wavelength) between the outgoing and returned modulation signal(s) is compared. Time-of-flight is calculated based on the phase-shift and the modulation signal frequency:

$$Time\ of\ flight = \frac{Phase\ Shift}{2\pi\ \times Modulation\ Frequency}$$

Adding multiple modulation frequencies can increase the accuracy of the time-of-flight calculations; however, practical limitations on the power output of continuous beam lasers limit the practical range to around 100 m (Kemeny and Turner, 2008; Petrie and Toth, 2008; Jaboyedoff et al., 2012)

- **Pulse method** scanners send out discrete laser pulses, and use time-of-flight measurements to calculate distance to a target; distance is calculated based on the simple relationship between travel time Δt and beam velocity, *c* (i.e. speed of light)

$$distance\ to\ point = \frac{c \times \Delta t}{2}$$

Scanners also measure amplitude of the reflected beam to assign an "intensity" value to each point, which depends on target reflectivity. Reflectivity in turn is affected by rock mineralogy, surface roughness, moisture, presence of vegetation, and beam angle of incidence (Sturzenegger, 2010; Jaboyedoff et al., 2012).

In this study LiDAR survey was undertaken using a tripod-mounted Optech ILRIS-3D (Figure 3 - 6). The ILRIS-3D is a time-of-flight scanner, and is capable of sampling 2000 points per second, with resolution as fine as 7 mm from a shooting distance of 100 m when set to the smallest available ground pixel size (Optech Inc., 2008).

Figure 3 - 6: Optech ILRIS-3D scanner mounted on tripod.

Appendix B.

Jwaneng Mine: Supplementary Investigation Data

1 Rock Mass Properties

Tables 4-1 to 4-3 summarise geotechnical parameters developed by SRK for the Cut 8 slope design assessment (Tunono et al., 2011; SRK, 2010). Table 4 - 1 summarises index properties, laboratory test results and rock mass classification estimates for the shale units intersecting the East wall, and Table 4 - 2 presents the estimated best-fit Mohr-Coulomb constitutive model parameters and elastic deformation parameters for the same units. Table 4 - 3 summarises estimated Mohr-Coulomb shear strength parameters for discontinuities within the quarzitic shale, including northwest-dipping foliation and sub-vertical tension joints. Both discontinuity and rock mass constitutive models were developed by SRK, following the approach of Little (1999) and Baczynski (2000, 2008) in considering the influence of near-surface blast-induced damage.

The blast damaged zone was assigned a thickness of T = 50 m back from the wall (Figure 4 - 1). The thickness *T* of the damage zone corresponds to the recommended value of $T = 2.5\ H$ where *H* = bench height = 20 m; from the guidelines suggested by Hoek (2012) and Hoek and Karzulovic (2000). The value of $T = 2.5\ H$ corresponds to large production blasting in a confined rock mass, with little or no control (i.e. worst-case blasting conditions). In fact, the blast damage zone may be limited by a smaller thickness of $T = 0.3$ to $0.5\ H$ with carefully controlled production blasts (i.e. with pre-splitting, buffer rows or other controlled blasting techniques) detonated towards a free face.

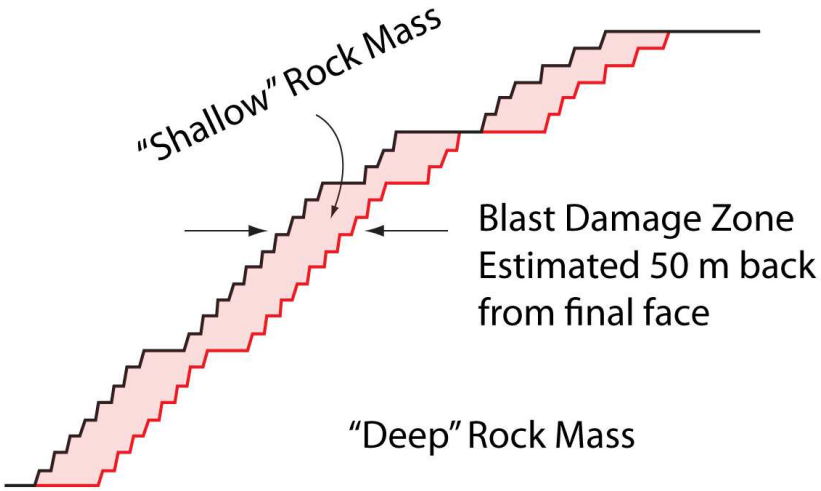

Figure 4 - 1: Blast damage zone approach of Little (1999) and Baczynski (2000, 2008; reproduced from SRK, 2009).

Table 4 - 1: Summary of shale rock properties from laboratory testing and field classification (Tunono et al., 2011; SRK, 2009, by permission).

	Timeball Hill Formation		**Rooihoogte Formation**
	Laminated Shale	Carbonaceous Shale	Quartzitic Shale
Density (kg/m^3)	2615	2616	2742
Intact Rock UCS (MPa)	56	115	173
RMR^{89}	44	54	60
GSI	39	47	47; *50 – 60*[1]
Hoek-Brown parameter m_i	3.3	4.9	5.2

[1]Ammended recommended GSI range based on field assessment in the current investigation.

Table 4 - 2: Summary of Mohr-Coulomb rock mass strength parameters and elastic deformation properties for shale rock units (Tunono et al., 2011; SRK, 2009, by permission).

	Timeball Hill Formation				**Rooihoogte Formation**	
	Laminated Shale		Carbonaceous Shale		Quartzitic Shale	
	Shallow Rock Mass	Deep Rock Mass	Shallow Rock Mass	Deep Rock Mass	Shallow Rock Mass	Deep Rock Mass
c (MPa)	0.13	0.30	0.35	0.65	0.5	0.86
φ (°)	23	20	37	32	40	36
σ_T (MPa)	0.10	0.12	0.15	0.17	0.3	0.35
E_{RM} (GPa)	1.6	2.1	1.7	2.3	3.9	5.3
Poisson's Ratio	0.26		0.25		0.25	

Table 4 - 3: Summary of Mohr-Coulomb discontinuity shear strength parameters for foliation and open sub-vertical joints (Tunono et al., 2011; SRK, 2009, by permission).

	Foliation		Open Tension Joints	
	Shallow Rock Mass	Deep Rock Mass	Shallow Rock Mass	Deep Rock Mass
c (MPa)	0.022	0.085	0.006	0.021
φ (°)	37	36	37	36

Appendix C.

Highland Valley Mine: Supplementary Investigation Data

1 Debris Accumulation and Bench Face Roughness

Preliminary assessments of debris accumulation and bench face roughness were carried out in order to assess post-processing techniques for evaluating slope performance. First, the low resolution (spot spacing = 15) point cloud was used to delineate major accumulations of debris. Next, bench face roughness was assessed for both the high resolution and low resolution point clouds, using the method of Lee (2011). Figure 6 - 1 highlights the debris accumulations from bench-scale failures, including three major piles, and also shows an overall-slope error map indicating bench roughness.

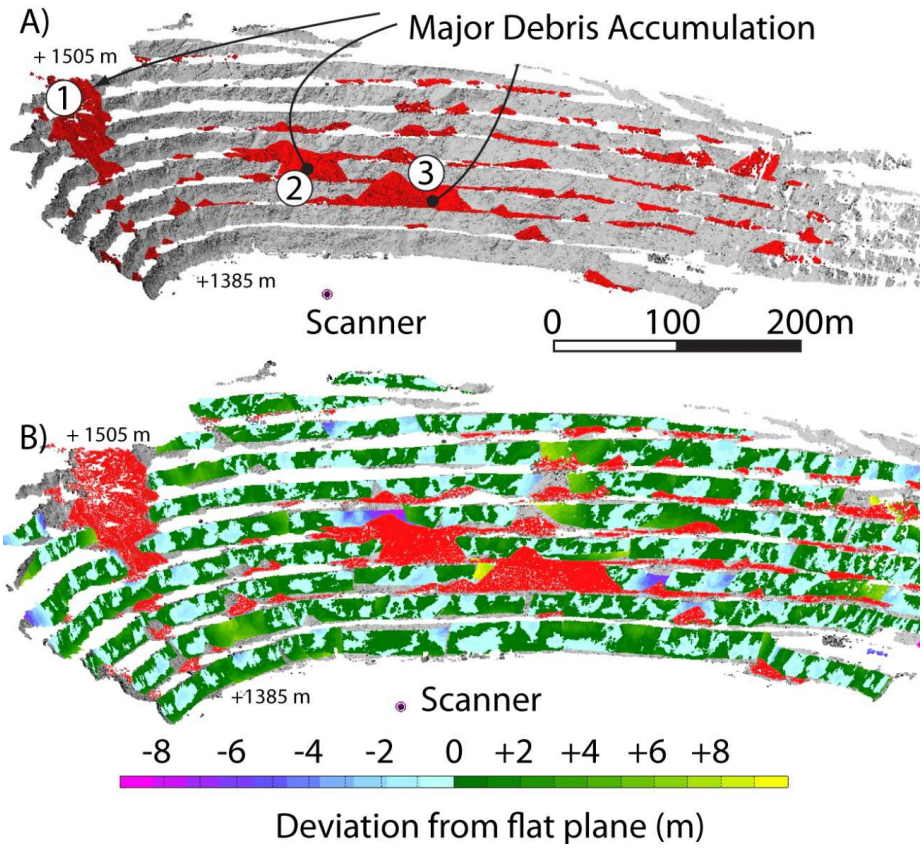

Figure 6 - 1: Perspective view of Upper West Wall, with highlighted regions showing major debris accumulation (A) and apparent bench face roughness (B), from low-resolution LiDAR point cloud.

The total volume of debris accumulated on the bench faces is in the order of 100 000 m^3. More precise assessment of the volume and severity of blast-induced overbreak and progressive bench crest loss could be attained by comparing the as-built LiDAR survey data to the mine design plan dimensions and blast pattern designs. Nevertheless, the height of major debris accumulations can be used as an indicator of reduced rock mass quality, and increased risk of rockfall (Lee, 2011).

Working areas below the three highlighted major debris piles in Figure 6 - 1 are the most probable zones of increased risk for rockfall. Using successive LiDAR scans to highlight areas of debris accumulation and bench crest loss may help with future consideration of rockfall risk, and may also be useful in consideration of appropriate remedial or mitigation measures.

The bench face roughness maps were derived using the error mapping function in PolyWorks (InnovMetric, 2006), based on the method of Lee (2011). Error maps representing the roughness of the bench faces (i.e. the deviation from perfect planarity) were derived in three steps:

> **Step 1:** Fit a rectangular plane to homogenous, approximately straight sections of bench face up to approximately 30 m long, until all bench faces are covered by best-fit planes.
>
> **Step 2:** Crop the fitted plane such that the surface covers the entire bench face, excluding major debris piles, because debris does not represent the in situ rock mass of the bench face, but rather post-mining topography resulting from progressive failure and blast damage.
>
> **Step 3:** Use the PolyWorks built-in “compare” function to compare bench planes to all data points in the point cloud; the resultant error map reflects the shortest distance from the best-fit plane to the LiDAR point cloud.

The preliminary roughness map derived from the low resolution survey (Figure 6 - 1) indicates that most of bench face area is approximately within ± 2 m from the local best-fit plane. Areas of greater roughness, in the range of -2 m to -6 m, associate with bench-scale wedge failures and block sliding failures, where the bench face has broken backward from the best-fit plane. Areas with the highest roughness, approaching -6 m to

-8 m, are associated with major debris piles. Taken together, the overall slope error map does not indicate a systematic pattern in bench face roughness.

To investigate the potential to interpret sub bench-scale structures, error maps from the high resolution survey (spot spacing = 7) were investigated at close range, from distances in the range of 10 m to 30 m. Figure 6 - 2 shows the overall error map for the entire high resolution point cloud, along with an inset from the RL + 1505 m bench face. Major planar joints belonging to set J1 are distinguishable in the roughness map by having similar error values, in the range of 0 to +2 m deviation from the best-fit plane. Step surfaces and lateral release surfaces formed by brittle blast-induced fractures (and in some cases pre-existing joints) are traced by the contours of roughness in the range of 0 to -2 m, receded behind the best-fit plane.

Sections of bench face with low or uniform roughness indicate good bench face performance, with uniform planar wall geometry. Rougher sections of bench face indicate complex or ragged geometry, where blasting damage has interacted with pre-existing discontinuities to create complex bench-scale wedge or sliding failures. In particular, negative roughness values in the range of 0 to -4 m indicate backbreak, where the as-built geometry has retrogressed into the slope from the best-fit bench face plane.

The error maps presented here represent an instantaneous assessment of bench face roughness. Comparison of the current bench roughness map with results of future LiDAR scans may help to assess the severity of progressive bench failure, and the time-dependency of overall slope performance in the Upper West Wall.

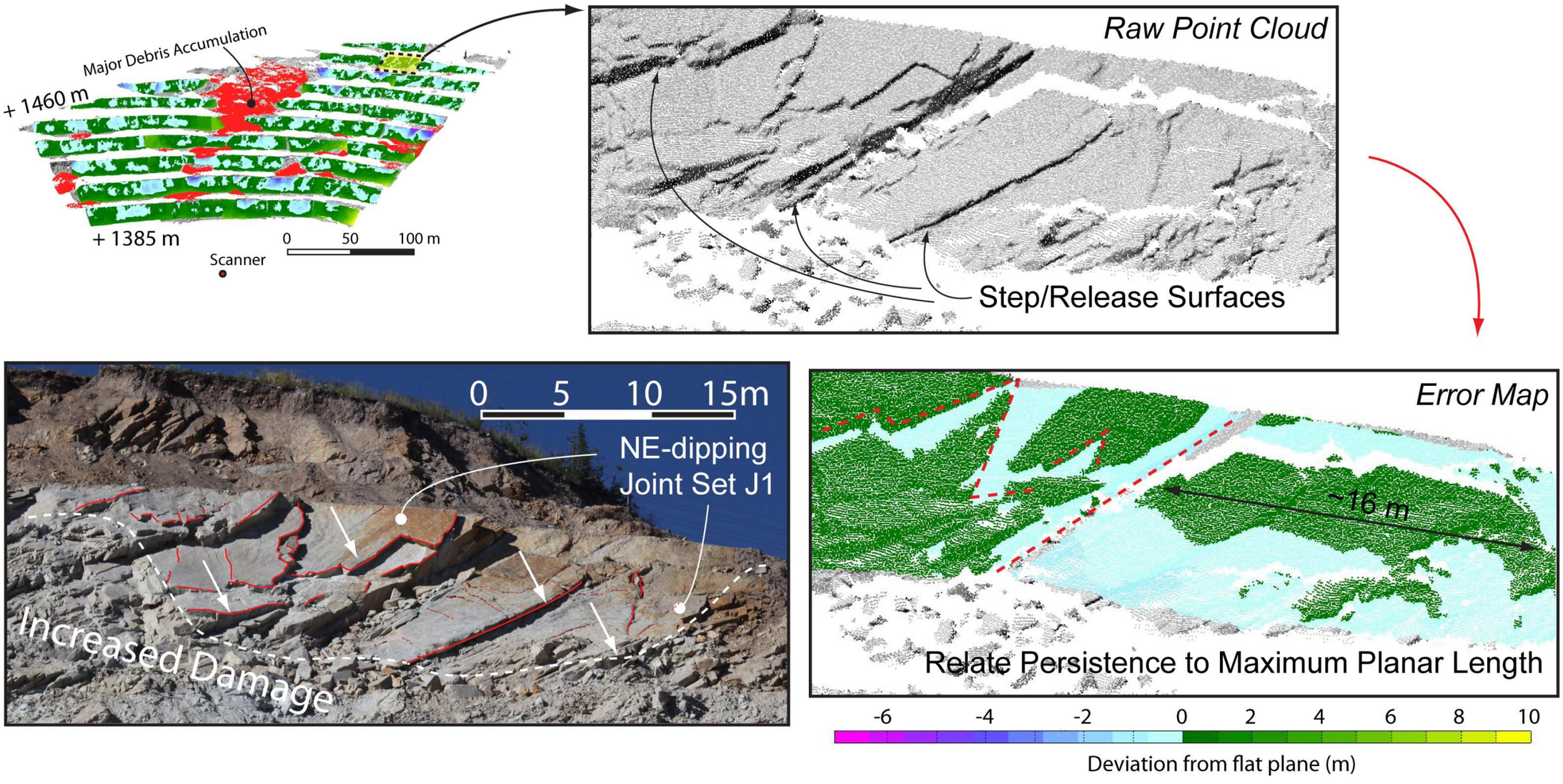

Figure 6 - 2: Characterization of bench face roughness from the high resolution LiDAR data, after the 3-D bench roughness method of Lee (2011).

2 Post-Processing with GIS

Preliminary post-processing of the LiDAR point clouds was carried out using ArcGIS, in order to investigate the benefit of GIS tools for characterising spatial trends in slope geometry and discontinuity structure. As a proof-of-concept exercise, both LiDAR scans were processed to produce contoured maps of slope steepness. Figure 6 - 3 presents a plan view of the overall Upper West Wall from the low resolution (spot spacing = 15; resolution = 5 cm to 20 cm) dataset, with insets from the high resolution (spot spacing =7; resolution = 1 cm to 10 cm) survey showing finer detail. Plan view insets from the high resolution survey show that the map can be used to characterise bench width variability and can also be used to extract bench face profiles for assessment of overbreak and bench slope performance.

Changes in slope steepness reflect the variation in bench face condition and geological structure. Lighter shades indicate more shallow dip angles, and darker shades indicate steep to sub-vertical dip.

Overall, the slope becomes flatter in Design Sector 3, where the largest accumulation of debris occurs. The transition boundary from steep bench face angles (red lines) towards shallower, failed benches (green) is delineated with dashed lines in Figure 6 - 3. Most of the bench-scale failures occur within Design Sector 3. The transition from the shallow, failed benches to steep bench faces occurs near the border between Design Sectors 2 and 3, which is also approximately co-located with the Yellow Fault.

The inset in Figure 6 - 3A demonstrates the potential to identify multi-bench scale geological structures based on changes in slope geometry, even if the feature itself may be obscured by debris. Figure 6 - 3B highlights the recurring “zig-zag” pattern resulting from blast-induced damage interacting with pre-existing discontinuities. In particular, there seems to be a tendency for backbreak to occur along northeast-dipping joints from set J1, in combination with brittle fracture induced by blasting.

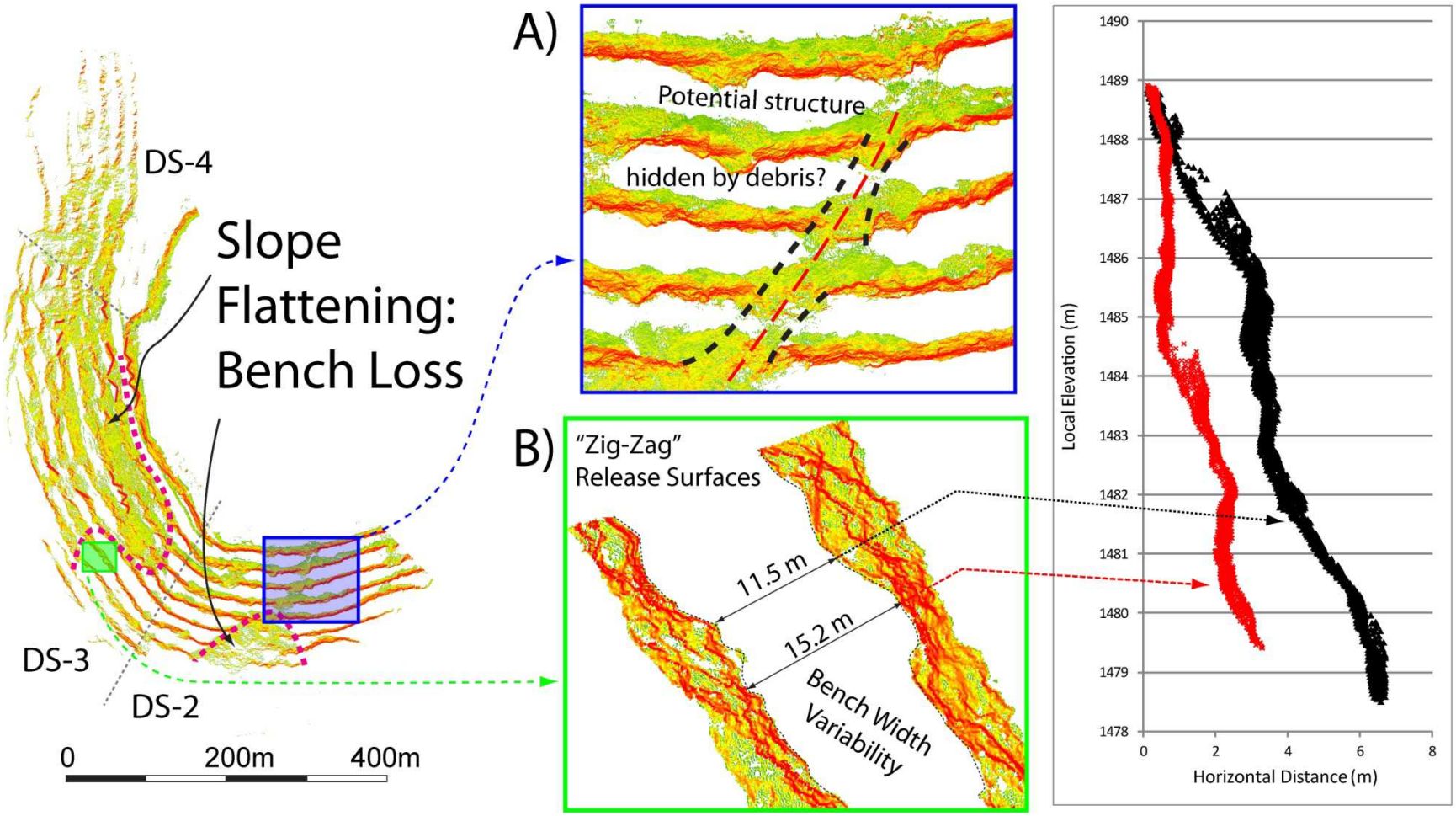

Figure 6 - 3: Slope steepness map and bench profiles created using ArcMap (Esri, 2012) from low resolution point cloud, with insets showing finer detail from high resolution point cloud; release surfaces, bench width variability (approximately 11.5 m to 15.2 m) and wall roughness in 2-D and 3-D can be assessed.

3 Characteristics of Bench Scale Wedge Failures

Bench scale failures occur throughout the Upper West Wall, with the highest concentration of failed rock mass occurring in Design Sector 3, shown in the LiDAR models by the height of accumulated debris in Section 4.3.3. Failures commonly involve sliding along discontinuities with intense phyllic or argillic alteration (indicating low frictional strength and pre-conditioning to shear failure) and release surfaces that show evidence of blasting damage and intact rock fracture. Basal sliding surfaces are commonly rough or undulating with amplitudes in the order of tens of centimetres to a metre, and wavelengths of up to 10 m.

Figure 6 - 4 shows an example of a wedge failure involving basal sliding on a sheared J5 discontinuity with potential influence of groundwater seepage. The release surface comprises a highly weathered, rough blast-damaged zone including intact rock fractures. Figure 6 - 5 shows another selected wedge failure with basal sliding along an undulating J1 discontinuity with a wavelength in the order of 10 m and a maximum amplitude of approximately 2.5 m indicated by the bench face roughness map.

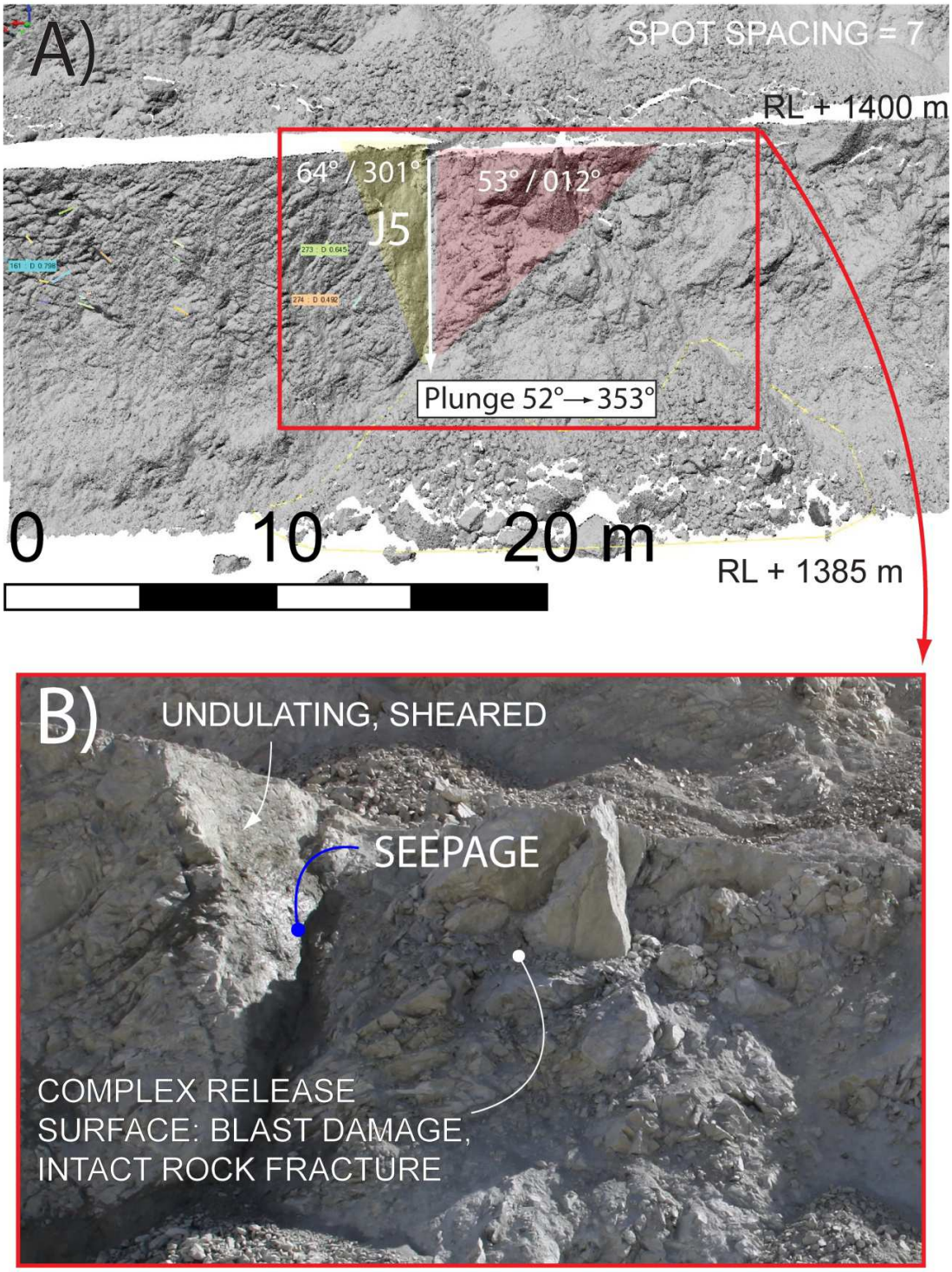

Figure 6 - 4: Bench-scale wedge failure in Design Sector 2, with an undulating J5 sliding surface with groundwater seepage; release occurs on complex blast-damaged and weathered surface with evidence of intact rock fracture.

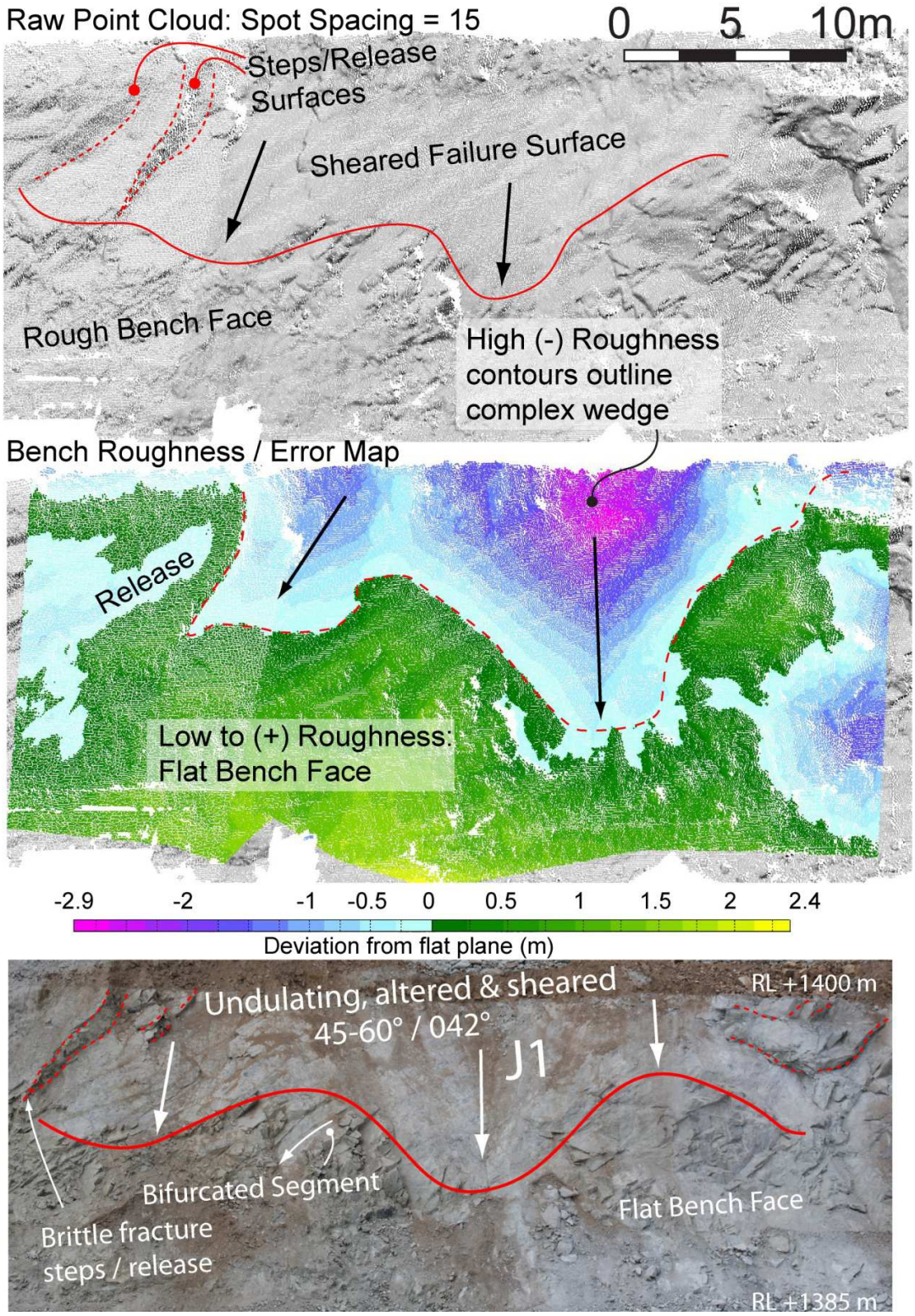

Figure 6 - 5: Bench-scale wedge failure in Design Sector 3, with sliding on undulating, altered and sheared J1 discontinuity; lateral release includes brittle fracture.

The field observations and LiDAR mapping indicate that wedge failure surfaces are rarely perfectly planar and persistent over the entire bench face. Most wedges involve two failure surface types:

1. **Primary Sliding Surface**: typically one discontinuity surface acts as a basal sliding surface, accommodating the majority of displacements. This plane may be undulating or curved, with visible groundwater seepage and phyllic or argillic alteration minerals present. The sliding planes often show evidence of shearing damage to primary roughness (asperities have been destroyed).
2. **Ragged/Complex Release Surface**: secondary surfaces provide kinematic release for sliding. Secondary failure surfaces are frequently discontinuous and ragged (i.e. high-relief surfaces), comprising a combination of blast-induced damaged and pre-existing joints: J1 appears to act as a common sliding surface while J2 to J5 may provide partial kinematic release.

To carry out preliminary assessment of bench scale wedge failure potential, the full population of discontinuity measurements from the combined LiDAR survey (n = 952) was imported into the limit equilibrium rigid wedge analysis program Swedge (Rocscience, 2011b). The full population of discontinuity measurements was used to investigate a potential “worst-case scenario” based on all major joint sets that may exist in the Upper West Wall. A less conservative analysis could be undertaken by sub-sampling the discontinuity measurements to include only local discontinuity sets in each design sector; however, this is a preliminary analysis only, intended to investigate a range of potential “what if” scenarios to illustrate the range of wedge geometries that may occur.

Using nominal bench geometry for Design Sector 3 (dip/dip direction = 70°/057°), a combinations analysis was undertaken to assess all possible discontinuity intersections, and the proportion of intersections that result in kinematically valid and failed wedges. The analysis was run for two base cases: the first case considers dry discontinuities, and the second considers water-saturated discontinuities. Figure 6 - 6 summarises the preliminary results.

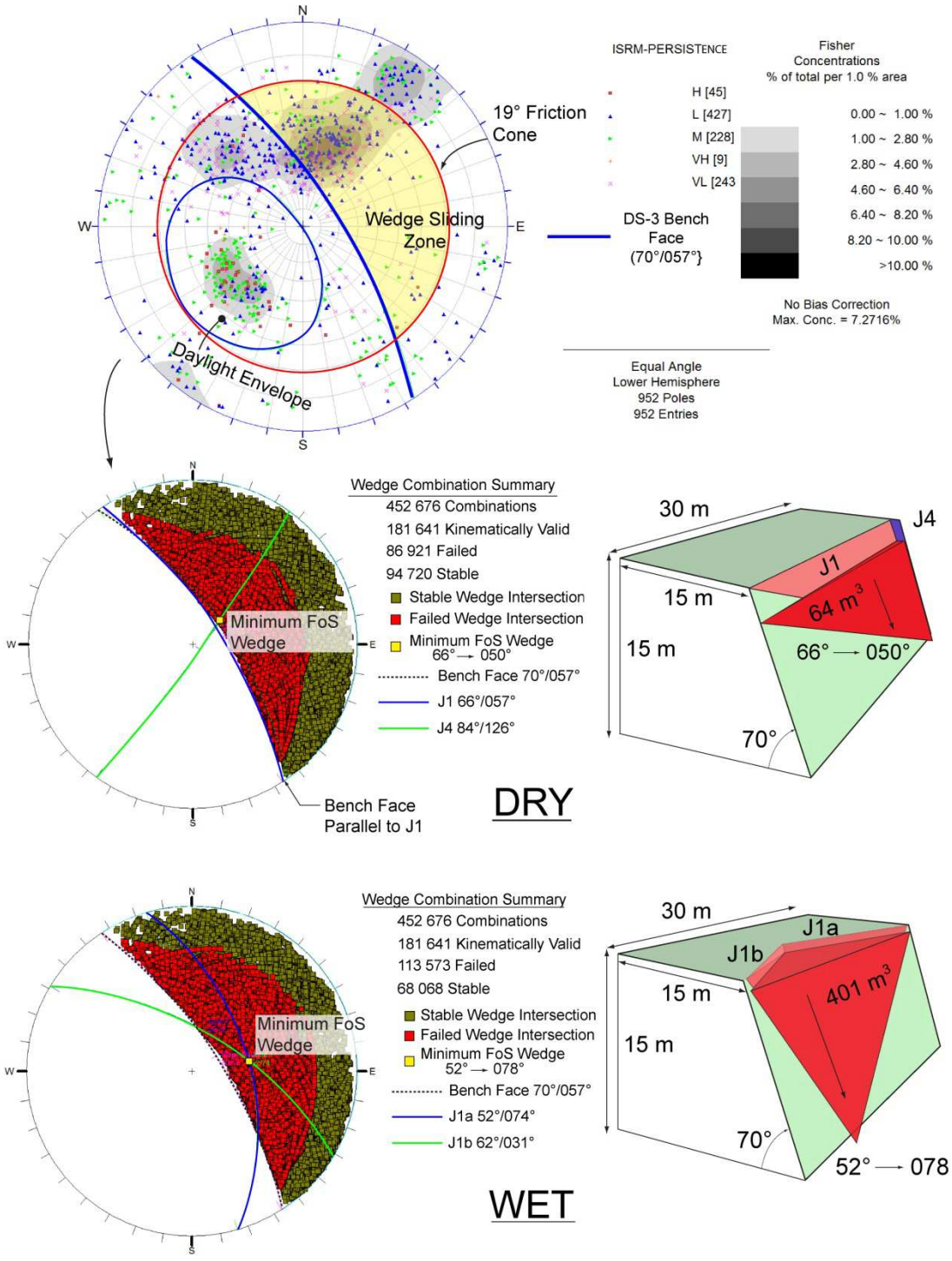

Figure 6 - 6: Preliminary combinations analysis of wedge failure potential based on nominal bench face geometry for Design Sector 3, for dry conditions and for reduced discontinuity shear strength with groundwater.

Joints were simulated as cohesionless, with friction angle of φ = 19° after the published values derived from investigations into the Lornex pit by Newcomen et al. (2003). Bench heights are idealized as the H = 15 m design specification, and bench width is W = 15 m, according to the typical bench widths noted in the LiDAR and ArcGIS plan figures. Strike length is limited to 30 m, based on the field observations that indicate that bench-scale wedge widths range from less than 5 m to a maximum of approximately 30 m along-strike. The results are filtered to exclude small wedges below a mass of 10 t (volume of 3.7 m^3). Although smaller wedges may present an important rockfall risk to staff and equipment, they are less significant in contributing to progressive backbreak and loss of bench width, unless backbreak is the product of multiple events.

Planes that intersect to form wedges inside the wedge failure zone are kinematically feasible and will fail, because they both (1) daylight in the slope and (2) have intersection lines that plunge steeper than the 19° friction angle.

The population of *n* = 952 discontinuities results in 452 676 plane intersections, of which 181 641 produce kinematically valid wedges (i.e. the intersection line daylights in the bench face). Under dry conditions, 86 921 combinations result in failed wedges, and there are 94 720 combinations that produce stable wedges. With the addition of pore pressure, the number of failed wedges is increased to 113 573, and the number of stable wedges is 68 068.

In the dry case, the critical wedge is triangular and flat, formed by a J1 discontinuity oriented sub-parallel to bench face, with lateral release along a J4 joint. The persistence of the J1 joint is 33 m. Although 33 m is slightly greater than the maximum persistence for J1 of 27.8 m identified in the LiDAR analysis, the difference is not significant enough to require wedge scaling to force realistic wedge geometry. The persistence of the J4 joint is 13.7 m, which is less than the maximum persistence for J4 of 18.2 m identified in the LiDAR survey. Based on the high to very high persistence of the joints, the wedge may be feasible only if discontinuities within the top 1% of persistence values are present. The wedge volume is 64 m^3. The flat wedge geometry and dominance of sliding on J1 is similar to field observations along the RL + 1385 m level (see Figure 6 - 5), where shearing was observed to occur along a very high persistence, undulating J1 discontinuity.

In the wet case (saturated fractures), the critical wedge is approximately pyramidal, formed by two discontinuities at the extreme ends of the J1 set window; the two joints are delineated J1a and J1b in this analysis, but they represent variably-oriented members of the same joint set. The persistence values of the J1 discontinuities forming the wedge are 27.4 m and 19.1 m; both values are less than the maximum J1 persistence of 27.8 m identified in the LiDAR survey data (Section 4.3.1), and thus may represent feasible geometry for wedges formed by J1 discontinuities within the top 1% to 5% of persistence values. The wedge volume is 401 m^3, an order of magnitude larger than the critical wedge computed for dry conditions.

The results indicate that where groundwater is present in adverse wedge-forming discontinuities, the number of failed wedges, and the failure volume of the critical wedge, is increased. However, care should be taken in interpreting the results of this simplified, kinematic rigid wedge analysis. The analysis considers joints as ubiquitous, and it does not consider the stabilising influence of lateral or rear constraint of wedges with intact rock bridges, nor are the de-stabilising influences of blast-induced damage and progressive, time-dependent crack growth (i.e. brittle creep) considered.

Recent studies into laterally constrained rock slides (Hungr and Amann, 2011) and overhanging rock slabs (Paronuzzi and Serafini, 2009) has demonstrated that release surfaces can be subjected to complex loading conditions including combinations of tensile stresses, bending moments and localized compression (Figure 6 - 7).

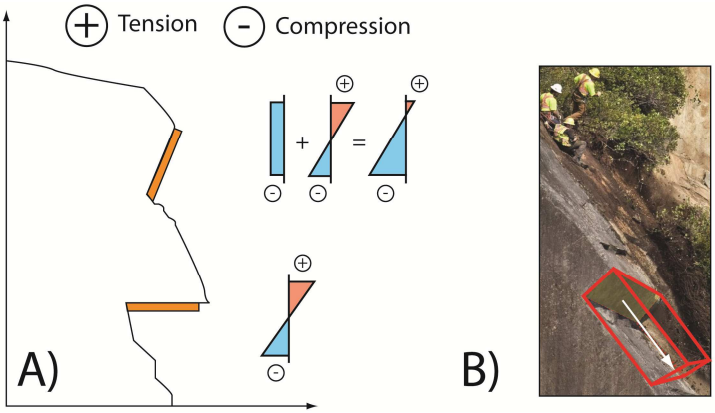

Figure 6 - 7: A) Hypothetical stress state of constrained release surfaces for hanging slabs (Modified and reproduced after Paronuzzi and Serafini, 2009); and B) Rear release of a planar sliding failure (Modified after Cross, 2008).

Initiation of bench scale wedge failure may thus be controlled by initial mode I tensile failure of intact rock leading to the creation of rear tension cracks and kinematic release surfaces. Alternatively, release may also develop through complex mixed-mode loading conditions (i.e. Mode I-II, I-III) leading to the creation of secondary brittle cracks features including bifurcation step surfaces, en echelon cracks, and irregular rough hackle fringes (Bahat et al., 2005). Prior to kinematic release, intact rock bridges may progressively fail under gravity loading, leading to increments of rotational block displacements or extensile strains, pulling blocks away from lateral release surfaces.

Tension cracks were observed in floor of the RL + 1400 m bench in Design Sector 3, near one of the field mapping locations (Figure 6 - 8). The tension cracks are curved, however the overall orientation is approximately parallel to the bench face, and they occur less than 100 m away from the wedge sliding failure surface previously pictured in Figure 6 - 5.

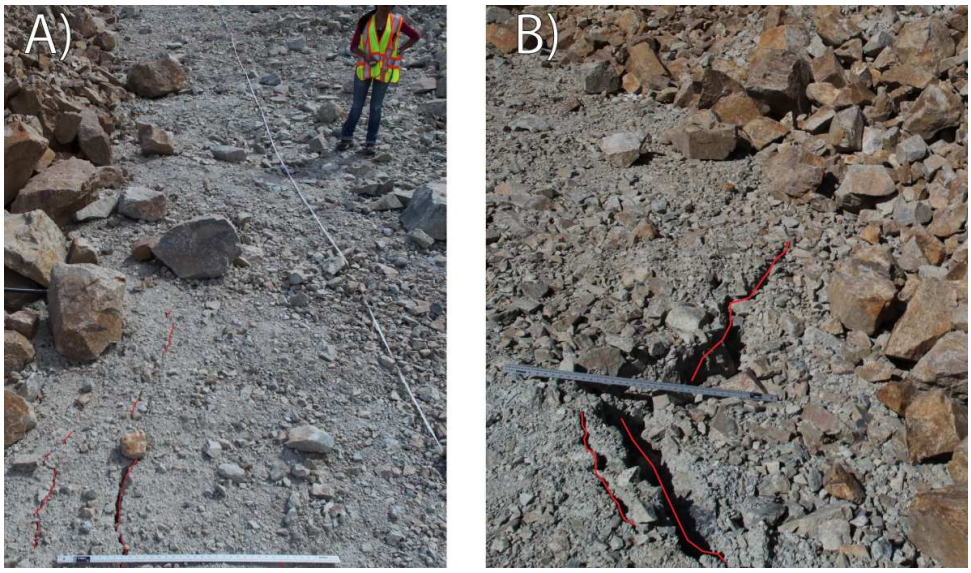

Figure 6 - 8: Tension crack development in floor of the RL + 1400 m bench looking south (A); and looking North (B).

Widening of tension crack aperture with time suggests sub-critical development of a kinematic release surface, and indicates progressive displacements of the unstable volume, accommodated by basal shearing along an undulating J1 (or similar) discontinuity. The precise geometry of the basal surface is difficult to determine before failure has occurred. However, observations of other nearby wedge failures suggest that

the unstable volume may be undergoing shear displacement via one of two likely mechanisms:

(1) Shearing along a medium or high persistence phyllic or argillic-altered J1-discontinuity (dip 40-60° toward northeast, approximately 045°) or
(2) Complex failure involving shearing along low to medium persistence joints from sets J1 to J5 and intact rock fracture including extensile opening or rotation away from constraint surfaces comprising intact rock.

In either case, intact rock bridge failure is likely to occur contemporaneously with increases in tension crack aperture. Furthermore, the cohesive strength imparted by interlocking of rough and stepped discontinuities may be progressively degraded if weak, altered asperities are sheared during displacement of the unstable wedge.

To investigate the influence of tension cracks on wedge-forming potential, two additional Swedge combinations analyses were carried out with the addition of a sub-vertical (85° dip) tension crack to provide rear kinematic release. The first analysis was run for dry conditions, and the second analysis includes water-saturated fractures. The preliminary results are summarised in Figure 6 - 9.

The total number of wedge combinations is the same as the previous analysis without tension cracks; the population of n = 952 discontinuities results in 452 676 intersections. However, with the addition of tension crack to provide rear kinematic release, many more discontinuity intersections are predicted to produce kinematically valid wedges, including wedges with intersection lines that plunge into the bench face. In the dry case, there are 382 142 intersections that produce kinematically valid wedges. In the wet case, there are 342 946 valid wedges, a smaller number of valid wedges than that computed for the dry case. The result is due to excess pore pressures occurring along the basal sliding surfaces of wedges that plunge into the bench face: in these cases, excess pore pressure acts to stabilise the wedge.

Figure 6 - 9 highlights how in the wet case, excess pore pressures result in predicted failure of wedges with intersection lines that plunge into the slope. Engineering judgement should be applied in such cases. The author recommends that any wedges with intersection lines plunging into the slope face should be excluded from the analysis.

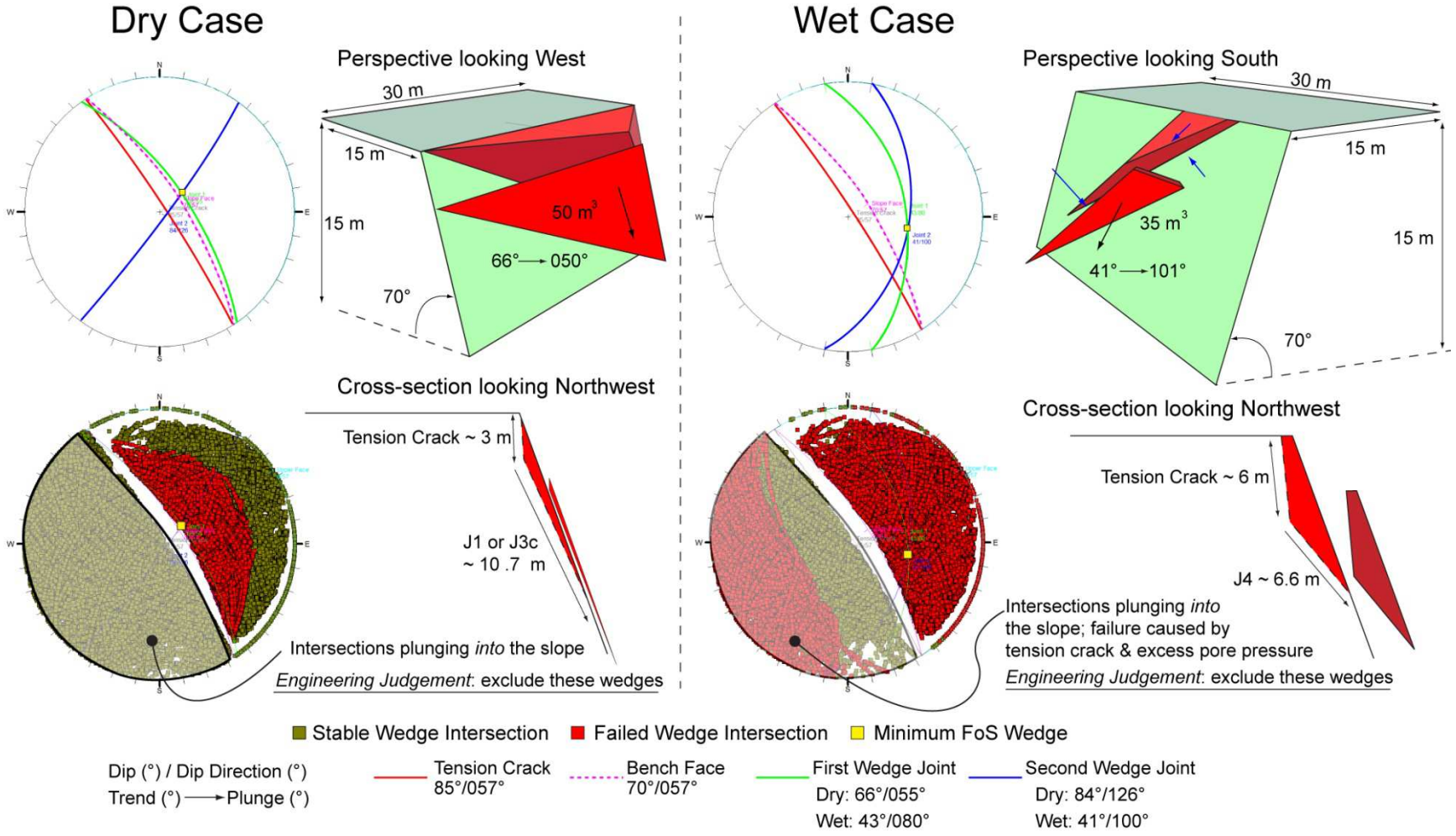

Figure 6 - 9: Summary of combinations wedge analyses based on nominal bench face geometry for Design Sector 3, including the sub-vertical tension cracks for rear kinematic release.

In the dry case 83 044 combinations produce failed wedges, out of 182 000 kinematically valid combinations with intersection lines plunging out of the slope. The result is similar to case with no tension cracks. In the wet case (water saturated fractures), almost 100% of wedges with intersection lines plunging out of the slope are predicted to fail.

In the dry case, the critical wedge is a flat triangular prism. Basal sliding occurs on a steep J1 or J3c discontinuity as identified in the LiDAR survey, oriented sub-parallel to bench face. Rear release is accommodated by the tension crack, and lateral release is provided by a J4 discontinuity. The persistence of the J1 joint is approximately 33 m, slightly larger than the maximum persistence for J1 of 27.8 m identified in the LiDAR mapping data. The persistence of the J4 joint is 13.7 m, which is smaller than the maximum measured persistence for J4 of 18.2 m, measured in the LiDAR survey. The critical wedge may be feasible only if discontinuities within the top approximately 1% of persistence values are present. The wedge volume is 50 m^3.

In the wet case (saturated fractures, tension crack is full of water), the critical wedge is elongated, approaching rod-like shape according to the ternary diagram-based block shape classification proposed by Kalenchuk et al. (2006). The wedge is formed by the intersection of J1 and a random discontinuity not belonging to any of the delineated sets J1 to J5. The persistence of the J1 discontinuity is 23.5 m, which is less than the maximum measured persistence of J1 identified in the LiDAR survey, 27.8 m. The persistence of the random joint is 18.2 m. The wedge volume is 35 m^3, which is smaller than the volume of the critical wedge computed for dry conditions. When the wedge is removed, the detachment niche results in an overhang in the remaining bench face.

The results indicate that when the presence of tension cracks is considered, additional kinematic freedom results in increased incidence of wedge failure. However, care must be taken in interpreting the results: the author suggests that wedges with intersection lines plunging into the bench face should be excluded from analysis. If discontinuities are saturated with groundwater, then almost all (> 99%) wedges plunging out of the bench face are predicted by Swedge to fail; however, this result represents a worst-case scenario where the wedge surfaces are comprised entirely of pre-formed joints that are

fully saturated, with no allowance for partial saturation and the role of intact rock bridges in strengthening the wedges.

Results from the Swedge analyses represent simplified low-level assessment of wedge forming potential. Tension cracks are idealized in this analysis as fully-formed, pre-existing structures. The analysis does not directly consider the stabilising influence of intact rock bridges along the rear release surface, nor is the formation of the tension cracks simulated as a time-dependent crack growth process (i.e. brittle creep) driven by gravity-induced stresses. The results reported here should not serve as a blanket assessment of wedge failure potential for the Upper West Wall, but rather as a preliminary investigation into potential “worst-case scenarios” for wedge failure potential, and the role of different discontinuity sets in forming sliding surfaces or kinematic release surfaces.

Field mapping indicated that bench-scale wedge failure surfaces are commonly dominated by low persistence discontinuities of 5 m or less, with frequent occurrence of blast-induced damage and intact rock fracture. If kinematic release is initiated by tensile failure of intact rock bridges, then a combination of mode I failure analysis with the negative exponential distribution for discontinuity persistence may be well-suited to characterising bench-scale instabilities.

Potential inter-ramp failures, conversely, have increased potential to be controlled by very high persistence shear structures (i.e. 20 m+). The negative exponential distribution for discontinuity persistence will tend to under-predict the rare occurrence of such high persistence features, and thus may not be well suited to characterisation of potential inter-ramp or overall slope instabilities. Inter-ramp and overall-slope scale stability assessment must rely on thorough geotechnical investigation in order to characterise important outlier structures with very high persistence that would not be predicted with statistical methods, such as segments of the Yellow Fault.